Lawrence Berkeley National Laboratory

Title

Ethanol-fueled metal supported solid oxide fuel cells with a high entropy alloy internal reforming catalyst

Permalink

https://escholarship.org/uc/item/83g439md

Authors

Hu, Boxun

Lau, Grace

Lee, Kevin X

et al.

Publication Date

2023-10-01

DOI

10.1016/j.jpowsour.2023.233544

Copyright Information

Peer reviewed

Ethanol-Fueled Metal Supported Solid Oxide Fuel Cells with A High Entropy Alloy Internal Reforming Catalyst

Boxun Hu[1], Grace Lau[1], Kevin X. Lee[2], Seraphim Belko[2], Prabhakar Singh[2], and Michael C. Tucker[1]

1. Energy Conversion Group, Lawrence Berkeley National Laboratory, Berkeley, CA 94720, USA

2. Materials Science and Engineering, University of Connecticut, Storrs, CT 06269-5233,

Abstract

High-performance metal supported solid oxide fuel cells (MS-SOFC) with an integrated high entropy alloy (HEA) internal reforming catalyst (IRC) are demonstrated for transportation applications using ethanol and methanol as fuels. Addition of the HEA IRC dramatically improves cell performance and stability when using ethanol/water blend fuel. Absence of carbon deposition predicted by thermodynamic calculations is confirmed by Raman spectroscopy analysis of posttest anodes. Optimal catalyst processing (deposition technique, loading, firing temperature) and cell operation conditions (flow rates, temperature, fuel compositions) are explored. Infiltrated HEA reforming catalyst provides a highly porous structure and low catalyst loading (6 mg cm^{-2}). The designed structure and catalysts achieve small mass transport resistances in the fuel electrode (26.2 sec m^{-1}) and oxygen electrode (41.6 sec m^{-1}). The best ethanol concentration (60:40 v% ethanol: water) provides 0.83 W cm^{-1} at 700°C, without carbon deposition. The ethanol-fueled MS-SOFC is operated for 500 h, including five thermal cycles. Cell evolution is similar to that reported previously for hydrogen fuel; nickel aggregation and chromia deposition were the major observed changes, and carbon formation can be avoided even after long-term operation.
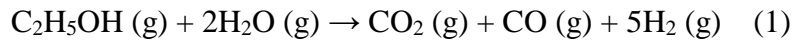
1. Introduction

Solid oxide fuel cells (SOFC) have demonstrated fuel flexibility, and high energy efficiency for co-generation of electricity and heat with reduced carbon dioxide emission [1]. In addition to hydrogen, various kinds of hydrocarbon fuels, such as natural gas (methane) [2], methanol [3], ethanol, biofuel, and coal, have been demonstrated via external steam reforming (ESR) or direct internal reforming (DIR) [4, 5]. Among these fuels, renewable bio-ethanol produced from agricultural feedstocks and algae is favored due to high energy density, easy storage and transport, and a low environmental impact. Currently, ethanol-blended fuel (≥ 10 % ethanol) is widely utilized for gasoline vehicles in the United States, Brazil, and Europe. Nissan's vision is to utilize ethanol for electric vehicle range extenders [6, 7]. Metal supported SOFCs (MS-SOFC), utilizing low cost ferritic steels as support, enable fast start and thermal cycling of the MS-SOFC power system, a key requirement for consumer vehicles [8-10]. Taking these advantages of MS-SOFCs and bio-ethanol, ethanol fueled SOFCs are being developed for electric vehicles using concentrated ethanol (≥ 45 v% ethanol/water (balance), abbreviated as "45% EtOH") as a fuel [11, 12]. Recent evaluation of the feasibility of ethanol and gasoline in SOFC vehicles indicates that ethanol fueled SOFCs have more economic, environmental, and social advantages than gasoline fueled vehicles [13].

DIR operation allows the steam reforming reaction (Equation 1) and fuel cell reaction (Equation 2) to proceed in sequence in the anode side, without the extra complexity, volume, and cost associated with external reformers. Additional DIR benefits include increased overall efficiency and inherent dynamic stability [14]. As fuel cell power is increased, more heat and water are produced, which are required for internal reforming. Hydrogen consumption by the fuel cell reaction thereby directly drives the steam reforming of ethanol forward. Steam produced in

reaction 2 returns to the outside of reforming catalyst layer and reduces the need for water injection. This allows high concentration of ethanol fuel in the storage tank, thereby increasing the driving range of the electric vehicle. Overall, the elimination of the external fuel reformer simplifies the overall power system design, lowers the cost, and increases the energy efficiency of the power system. The shortcomings of DIR operation are inability to replace the DIR catalyst, and limited space for catalyst. Therefore, the selected DIR catalysts are required to be durable and highly efficient.

$$C_2H_5OH \text{ (g)} + 2H_2O \text{ (g)} \rightarrow CO_2 \text{ (g)} + CO \text{ (g)} + 5H_2 \text{ (g)} \quad (1)$$

$$H_2 \text{ (g)} + O^{2-} \rightarrow H_2O \text{ (g)} + 2e^- \quad\quad\quad\quad\quad (2)$$

Formation of carbon or coke during DIR is a primary concern for cell stability. Carbon deposition in the anode can block the electrode pores, deactivate catalyst sites, and lead to rapid cell breakdown in the worst cases [15]. Formation of carbon or coke (CnHm) can be predicted by thermodynamic analysis based on fuel/steam ratio, operating temperature, type of solid electrolyte and extent of the electrochemical reaction of hydrogen [16, 17]. Many attempts to produce carbon-tolerant internal reforming catalyst have been made [3, 18-22]. Cu-YSZ [23], Co-Cu bimetallic [24], precious metals (Pd, Pt, Rh) doped Cu-CeO$_2$ [25] have been developed as carbon resistive catalysts and the cell performance has been improved from about 0.1 W cm^{-2} to 0.3 W cm^{-2} using methane fuel at 700°C. Although Cu-based anodes are quite resistant to carbon deposition, they suffer low cell performance due to lower activity than standard Ni catalysts. There are also several previous reports of ethanol internal reforming. A CeO$_2$-Co$_3$O$_4$-CuO anode produced 0.16 W cm^{-2} with anhydrous ethanol as fuel at 850°C [26]. Dogdibegovic et al reported that a Ni-SmCeO$_2$ (Ni-SDC) anode-based cell generated a constant power of 0.28 W cm^{-2} for 100 h (active cell area corrected) using 45% EtOH fuel at 700°C [7]. A Ni-YSZ anode-based cell integrated with a

reforming catalyst layer of $La_{0.4}Sr_{0.6}Co_{0.2}Fe_{0.7}Nb_{0.1}O_{3-\delta}$ (LSCFN) with anchored nanoscale Co-Fe alloy produced 0.28 W cm^{-2} at 700°C using 60 v% ethanol/N_2 (balance) [27]. These coke-free catalysts benefit from low Ni loading and well-dispersed Ni nanoparticles supported on ceria and low concentration of ethanol [28]. However, Ni-SDC anode is prone to carbon deposition at higher concentration of ethanol (> 45 v% EtOH).

High entropy alloy (HEA) reforming catalysts, which contains 5 or more elements with concentrations between 5-35 atom%, expand conventional alloying approaches for functional catalysts [29]. Lee et al. reported that HEA-GDC reforming catalyst delivered superior operation stability without coking or carbon deposition in the anode using methane fuel for 30 h [30]. The HEA shows advantages (resistance to coke formation and sintering) over conventional bi-alloys of Ni, Co, Cu, Fe and Mn elements. Some of the challenges associated with introducing internal reforming catalysts (other than HEA) into MS-SOFCs were affinity to metal support, loss of surface area due to sintering, and deleterious interaction with SOFC components [31]. Our team previously developed HEA for methane and successfully integrated it into MS-SOFCs with gaseous fuels [2]. MS-SOFCs with HEA-GDC reforming layer achieved 0.5 W cm^{-2} using 97% CH_4/3% H_2O fuel without carbon deposits or coke after 40 h operation. Here, we extended the use of HEA reforming layer on MS-SOFCs to high-concentration ethanol liquid fuel.

This study demonstrates HEA-SDC internal reforming catalyst for improving cell performance and stability. The HEA-SDC catalyst is integrated onto our recently optimized MS-SOFCs (with thin and highly porous metal supports) via infiltration and brush paste methods [32]. The impact of the HEA-SDC reforming catalyst loading and thickness, and the operating temperature on the

cell performance are explored. Mass transport of the HEA-SDC/Ni-SDC-based MS-SOFC is quantified and electrode morphologies are analyzed with scanning electron microscopy. Carbon deposition is predicted by thermodynamic analysis and confirmed by cell testing results. The stability of the ethanol-fueled MS-SOFCs are tested for up to 500 h. Degradation factors such as catalyst agglomeration and chromia deposition are analyzed. Alternate fuels such as methanol are also tested with HEA catalysts. This study provides useful information for further development and commercialization of ethanol-fueled MS-SOFCs with IRC.

2. Experimental Methods

2.1. Cell Fabrication

The optimized cell structure and catalyst infiltration protocol developed recently with hydrogen fuel was utilized for the cell fabrication in this study [32], with the exception of Figs 6c/d, S1, and S5, which used the previous generation of metal support structure. Symmetrical MS-SOFCs (~2.6 cm diameter) were prepared by tape-casting, lamination and sintering. Prior to catalyst infiltration, cells were oxidized in air at 850°C for 4 h to increase wetting of the catalyst precursor solutions and provide a continuous protective Cr-oxide scale. Pr_6O_{11} cathode was infiltrated 8 times and Ni-SDC (40 vol% Ni-60 vol% Sm) anode was infiltrated 9 times. After each precursor infiltration of both anode and cathode, the cell was fired rapidly on a porous zirconia support at 800°C for 30 min in a box furnace. The flat symmetrical cell endured rapid thermal cycles without delamination. Details of the procedures are described in our earlier report [32].

Before infiltration of HEA-SDC reforming catalyst at the anode side, platinum mesh was spot welded to the anode metal support for current collection. HEA-SDC internal steam reforming catalyst was added to the anode by infiltration or brush painting. For infiltration of HEA-SDC

catalysts, stoichiometric mixtures of Co, Fe, Cu, Mn, Ni-, Sm-, and Ce-nitrates (Sigma Aldrich) were mixed with glycine, Triton-X surfactant and deionized water and stirred overnight to obtain a clear HEA-SDC nitrate precursor solution. Initial Co:Mn:Cu:Fe:Ni nitrate (containing crystal water) weigh ratio is about 7:2:4:11:7. The HEA-SDC nitrate solution was dripped onto the anode, followed by application of vacuum (400 mbar) to remove air in the metal support, and dried at 90°C for 15 minutes. The infiltrated cells were directly placed in a hot furnace (850°C) for 30 min. A typical HEA catalyst loading is 6 to 12 mg cm^{-2}. For brush painting of HEA-SDC catalysts, a thin layer of HEA ink (40:60 wt powder: ink vehicle (FuelCell materials)) was painted onto the anode using a brush followed by calcination at 850°C for 2 h in air. Synthesis of HEA-SDC powder is described elsewhere [30]. The infiltration method produced better cell performance than the painting method for loading HEA-SDC reforming catalysts, and was therefore selected for the cells reported here (see Supplementary Information, Fig. S1).

2.2 Cell testing

Button cells were mounted onto 410 stainless steel test rigs with spot-welded Pt wires/mesh connecting the cell to the electrochemical testing interface using a 4-probe method (Fig. S2). Alumina fuel transport tubes (6 mm diameter) were inserted inside the stainless-steel inlet and outlet tubes to avoid carbon formation in the intermediate-temperature sections of the test rig. Glass powder was applied as a paste (Schott GM31107 mixed with terpineol) by syringe to the edges of the cells and heated to 90°C at 10°C min^{-1}, then to 200°C at a ramp rate of 2°C min^{-1}, and finally to 700°C at a ramp rate of 10°C with a dwell time of one hour. The cell supported on a test rig was placed in a two-inch diameter alumina tube (with one end open). The open end was stuffed with insulating alumina fibers (Zircar). For safety, the anode was then flushed with N$_2$ (or Ar)

7

before introducing 150 cm^3 min^{-1} hydrogen fuel (97% H$_2$/3% H$_2$O). The cathode was supplied with air flowing at 500 to 1200 cm^3 min^{-1}. Ethanol/water blended fuel (45 to 95% EtOH) was injected to a 50 mL stainless steel buffer tank (Swagelok) using a syringe pump (Harvard). The buffer tank and inlet tubes were wrapped with heating tape to keep the ethanol/water stream above 120°C. During thermal cycles (700-250-700°C), the anode chamber was flushed with nitrogen, to avoid solid carbon deposition which is thermodynamically favored below 650°C. Dry simulated reformate corresponding to 45% EtOH (70 v% H$_2$, 16.7 v% CO, 12.5 v% CO$_2$, and 0.8 v% CH$_4$) was passed through a water bubbler heated by silicon oil bath at 61.5°C (24.5 v% water) to check reforming efficiency. Open circuit voltage (OCV), electrochemical impedance spectroscopy (EIS) at OCV and 0.7 V, and cell performance (IV-PI and I-t) were assessed with a multichannel potentiostat with current boosters (Biologic VMP3 with 10 A boosters).

2.3 Characterization

Scanning Electron Microscopy - Energy Dispersive X-ray Spectroscopy

Select fresh or posttest cells were mounted in low-viscosity epoxy, cut, and polished to prepare for structural analysis using a scanning electron microscope (SEM). To analyze electrode catalysts, one metal support was peeled off to expose the ceramic layers. High-viscosity epoxy was dripped on the exposed electrode layer and dried at room temperature overnight. The epoxy sample was pulled off the remaining metal support, and cut by a razor to create a fracture section of the ceramic layers. Field emission scanning electron microscopy (FESEM) images were collected using a Zeiss Gemini Ultra-55 instrument with an in-lens and quadrant backscatter detector at a voltage of 20 kV. An energy dispersive X-ray (EDX) detector with a beam energy of 20 kV was used for element analysis.

FIB-STEM

High-resolution scanning transmission electron microscopy (HR-STEM) was performed on a Talos 200 S/TEM (Thermo Fisher Scientific) for high resolution images and element analysis.

X-ray diffraction

High temperature-XRD (HT-XRD) was performed using an automated multipurpose X-ray diffractometer equipped with an Anton Paar high-temperature oven chamber and SmartLab Studio II software. HEA-SDC catalysts were pre-calcined in a box furnace at 400°C to avoid off-gassing into the XRD chamber. HEA/SDC powders were heated on the XRD stage in air or 3% H_2/Ar (balance). The powder was heated from 400°C up to 850°C at a ramp rate of 20°C with a dwell time of 15 minutes at each measured temperature. The HT-XRD scanned the sample with a speed of 5°C min^{-1} at a step of 0.01° and 2Θ range from 20 to 80 degree.

Raman Spectra

After operation, the metal supports were peeled apart and the HEA-SDC and Ni-SDC anodes were analyzed for carbon deposition using a Renishaw InVia Qontor Raman system spectrometer with 433 nm (and 633 nm) lasers equipped with a 50x magnification lens.

3. Results and Discussion

3.1 Catalyst Structure and Morphologies

The phase behavior of HEA oxide/SDC and HEA/SDC fired in air and followed by reduction in 3% H_2/Ar was studied by high temperature XRD to find optimal temperatures for infiltrated catalyst preparation. Fluffy and loose powder formed after HEA/SDC infiltration solution was dried at 120°C and calcined at 400°C in air. The powder was grinded and mixed well for HT-XRD. HEA oxide (JCPDS 10-0325) and SDC (JCPDS 75-0161) phases were formed (Figs. 1a and S3a).

Three separated XRD peaks of HEA oxide at 35.5°, 43.3°, and 63.1° have apparent peak broadening due to high disorder and small crystallite size, and peak splitting due to secondary phase, similar to other HEA compounds [33, 34] (Fig. S3 c, d). HEA peak intensities were lower than those of SDC peak intensities. These HEA/SDC nanoparticles have high surface area (> 35 m^2/g) [30]. HEA oxides presented in the form of cubic spinel phase AB_2O_4 (A: Ni, Cu, B: Fe, Co, and Mn, JCPDS 10-0325), similar to $NiFe_2O_4$ [35]. Peaks assigned to cubic fluorite phase of SDC were clearly observed. With increasing firing temperature up to 850°C, the intensity of HEA oxide peaks at (200), (220), and (310) increased and peak splitting disappeared, indicating that pure HEA-oxide phase formed (Fig. S3a). STEM-EDS maps of HEA oxide after calcining at 850°C in air shows overlap of the five element distributions (Mn, Fe, Ni, Co, and Cu), indicating that each element was almost evenly distributed (Fig. S4). Mn was somewhat less evenly distributed than the others, with some segregation observed. When the HEA-SDC powder was reduced in 3% H_2/Ar, HEA oxide peaks gradually disappeared and the intensity of HEA peaks (JCPDS 47-1417) increased (Figs. 1b, S3b). Complete conversion of HEA oxide to HEA was observed by 650°C (Figs. 1b, S3b). Two peaks at 43.6° and 50.8° were observed in the XRD pattern of the reduced sample, which are assigned to the (111) and (200) planes of HEA, similar to FeNi alloy [35, 36]. The volume of the HEA powder was visibly reduced by approximately half after HT-XRD due to loss of oxygen, and possibly sintering.
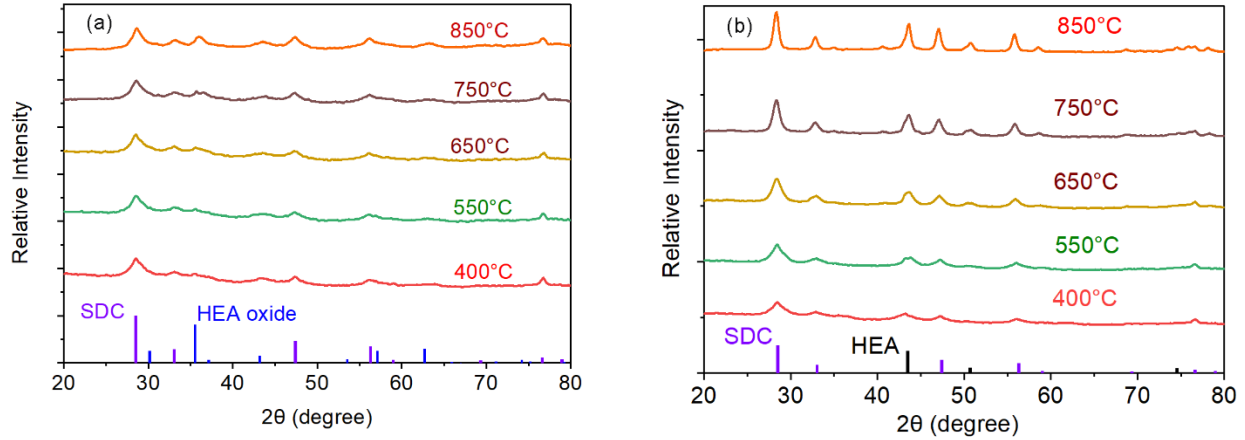
Fig.1. HT-XRD patterns of HEA/SDC (60:40 wt%) in (a) air and (b) 3% H_2/N_2. Standard patterns: HEA oxides (JCPDS:10-0325, blue line), SDC (JCPDS: 75-0161, magenta line), HEA (JCPDS: 47-1417, black line).

Infiltrated HEA oxide-SDC catalyst was uniformly coated at the ScSZ electrode backbone (Fig. 2a). After reducing in hydrogen and operation in 60/40 ethanol/steam for 100 h, the HEA-SDC layer shrank and a highly porous catalyst structure was observed on top of the anode near the metal support. HR-STEM images of pretest and posttest catalyst showed different morphologies and lattice structures (Figs. 2b, 2c, and S4). High resolution TEM imaging of HEA oxides shows a space fringe d (220) of 0.299 nm, slightly larger than that of $NiFe_2O_4$ of 0.28 nm [37]. The space fringe d (110) of HEA was 0.203 nm, close to the reported space fringe d (110) for NiFe (0.205 nm) [36].
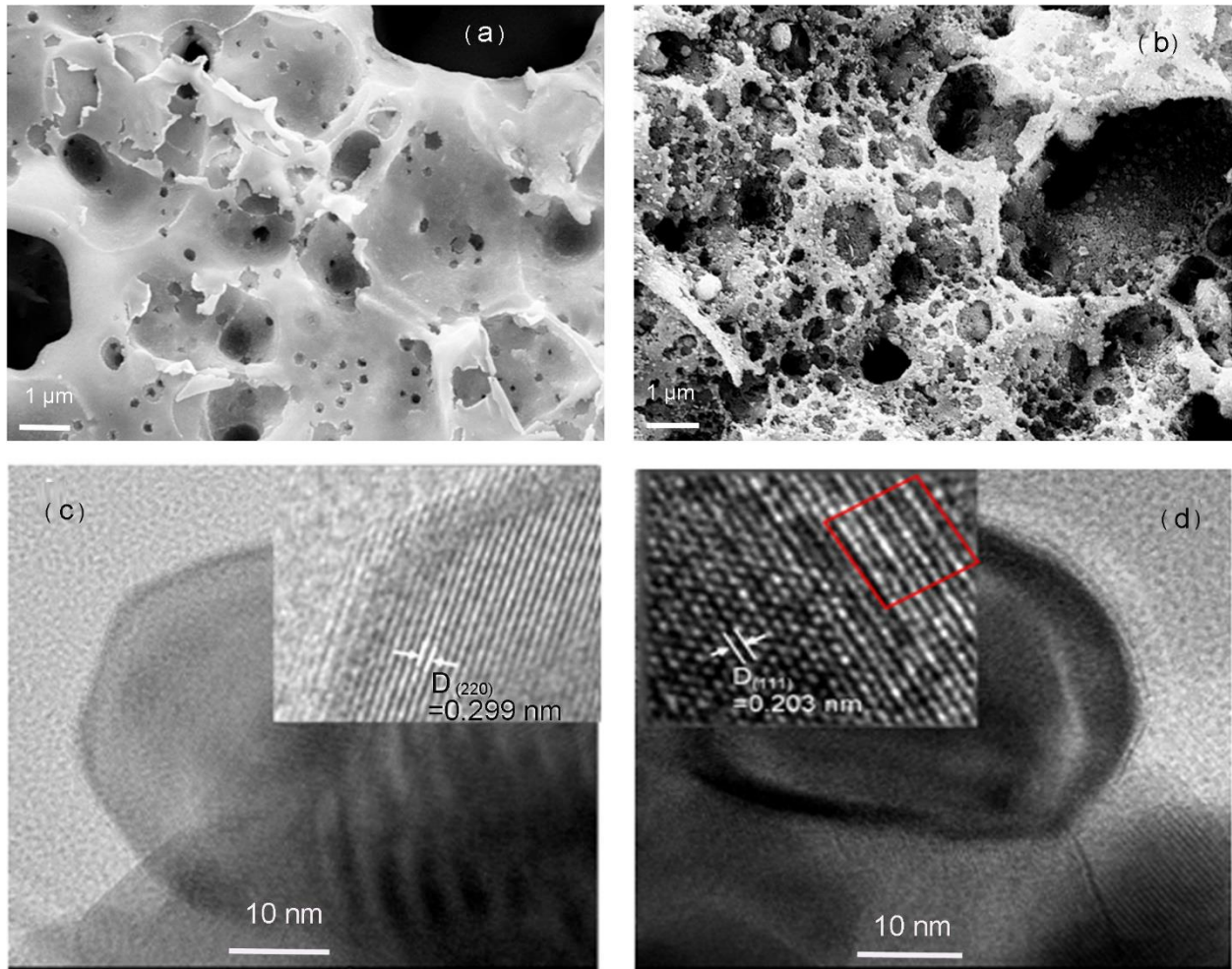
Fig. 2. HR-SEM and HR-STEM images of the HEA-SDC reforming catalysts. (a) HR-SEM image of HEA oxide-SDC, (b) HR-SEM image of the posttest and reduced HEA-SDC, (c) HR-STEM image of high entropy oxide, calcined in air at 850°C, (d) HR-STEM of posttest HEA in DIR-SOFC.

Addition of HEA-SDC reforming catalyst to the MS-SOFC anode improved P_{max} by 34% from 0.62 to 0.83 W cm^{-2} at 700°C using 60% EtOH (Fig. 3a) due to increased OCV and reduced cell impedance (Fig. 3b). The OCV increased from 1.01 V (Ni-SDC catalyst only) to 1.04 V (theoretical OCV: 1.04 V, Fig. 8b) using additional HEA-SDC reforming catalyst. The OCV is an indicator of extent-of-reforming, so this indicates that internal steam reforming was enhanced [7,

38] and the full theoretical concentration of hydrogen was generated by reforming in the presence of HEA-SDC. The Ni-SDC cell failed after about 24 h and obvious carbon deposition was visible. The HEA cell showed better stability (34.6%/65 h of HRA-SDC vs 44.8%/20 h of Ni-SDC) with much less degradation (Fig. 3c). No carbon was observed on the HEA-SDC cell by visual and Raman analysis, discussed in Section 3.5.
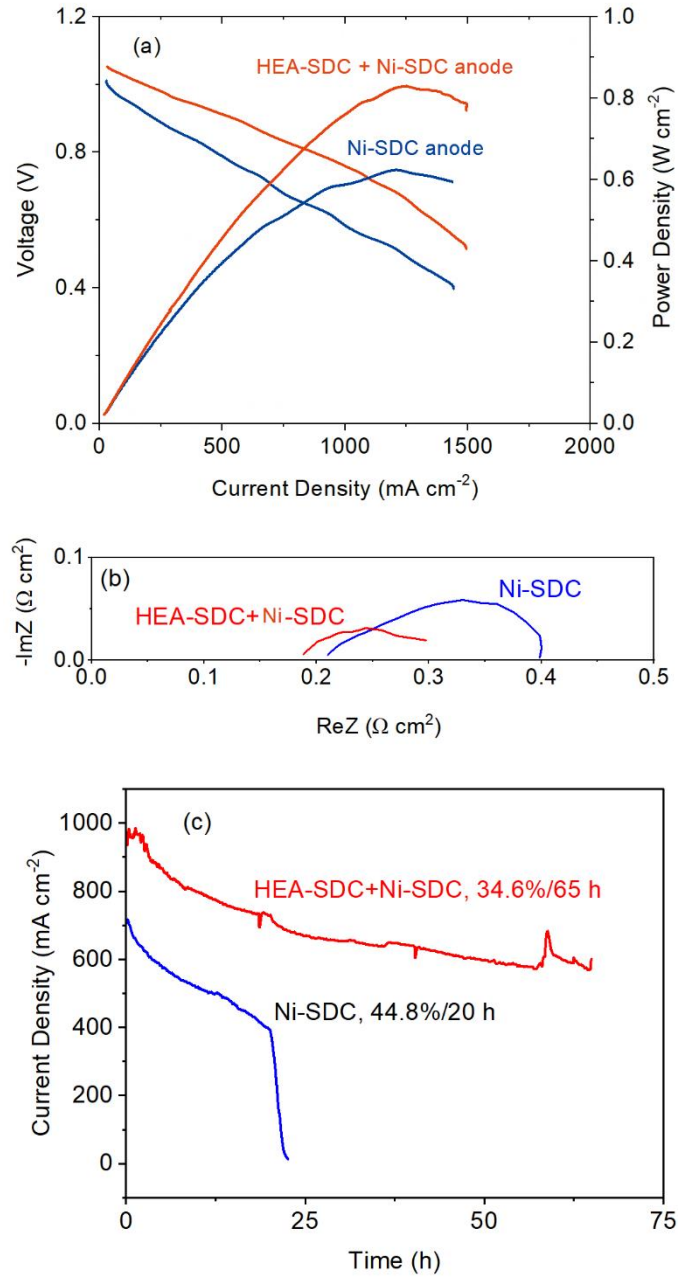
Fig. 3. Cell performance comparison of Ni-SDC and HEA-Ni-SDC anode-based cells, a: VI-PI curves, b: EIS at 0.7 V, c: I-t curves with a constant cell voltage of 0.7 V. Other cell testing conditions: 700°C, fuel flow: 6 mL h^{-1} 60 % EtOH, air flow:1.2 L min^{-1}.

3.2. Optimization of HEA and operation parameters

Several features of the reforming catalyst (HEA/SDC ratio, total loading) and operating parameters (fuel and air flowrates, ethanol/water ratio) were optimized. The HEA/SDC weight ratio was varied between 60:40 and 40:60; the best performance was found for 60:40 so this was selected for all further cells (Fig. S5a). The HEA-SDC loading was controlled by the number of infiltration cycles. One infiltration produced poor performance (low OCV and high ASR). Performance was improved for 2 or 3 infiltration cycles and the performance was similar for both (Fig. S5b). To reduce the HEA cost and avoid blocking the metal support pores, 2 infiltrations was selected for all further cells, yielding a reforming catalyst loading around 6 mg cm^{-2} for the optimized metal support. The optimal ethanol flow rate was 6 mL min^{-1} (Fig. S6a), although cell performance was not very sensitive to fuel flow rate. Cell performance was much more sensitive to air flow rate, due to oxygen mass transport limitation in the air-side metal support as discussed in detail previously [32]. Air flow rate of 1.2 L min^{-1} was required to avoid concentration polarization (Fig. S6b).

An optimized cell was tested with increasing ethanol: water ratio from 45 to 95% EtOH (Fig. 4a). The highest cell power (0.83 W cm^{-1}) was obtained using 60% EtOH fuel. Lower ethanol content generated a low hydrogen fraction and therefore a low OCV. Higher ethanol content led to unstable OCV and visible carbon deposition which presumably deactivates the catalyst. The internal reforming efficiency of an HEA-SDC based MS-SOFC was evaluated by comparing DIR

with 45% EtOH to a simulated reformate gas representing the same 45% EtOH fuel after being completely reformed (Fig. 4b). Cell performance of 45% EtOH fuel (Pmax: 0.62 W cm^{-2}) is only slightly lower than that using reformate (Pmax: 0.69 W cm^{-2}), suggesting that the DIR reaction is nearly complete. Temperature-dependence of cell performance was observed in the range of 600 to 800°C using another cell with moderate performance (Fig. 4c). The peak power was 0.23, 0.4, 0.57, 0.76, and 0.93 W cm^{-2} at 600, 650, 700, 750, and 800°C, respectively. This compares quite favorably with previous reports of SOFCs with DIR of ethanol. A similar cell tested in hydrogen fuel delivered the peak powers 0.36, 0.54, 0.87, and 1.1 W cm^{-2} at 600, 650, 700, and 750°C, respectively (Fig. S7), about 25% power increase was observed in hydrogen fuel. A cell with Ni-YSZ/Cu-CeO$_2$ DIR layer obtained a power density of ~0.4 W cm^{-2} at 7.3 vol% ethanol at 800°C without coking in short-term operation [39]. A simulation showed that La$_{0.75}$Sr$_{0.25}$Cr$_{0.5}$Mn$_{0.5}$O$_{3-d}$ (LSCM)-anode-supported cell at 750°C achieves a calculated power density of 0.51 W cm^2 with steam/ethanol ratio of 7 [40]. A Ni-ScSZ/ScSZ/GDC/LSCF cell integrated with La$_{0.4}$Sr$_{0.6}$Co$_{0.2}$Fe$_{0.7}$Nb$_{0.1}$O$_{3-\delta}$ (LSCFN) and Co-Fe alloy delivered 0.28 W cm^{-2} at 700°C using 60% EtOH/N$_2$ [27]. A Ni-YSZ/LSCF cell integrated with 5 wt% Rh/ CeZrO$_2$ DIR catalyst showed a Pmax of 0.26 W cm^{-2} using 35% EtOH at 800°C [12]. A direct ethanol anode-supported SOFC with nanosized Ir-Ga doped CeO$_2$ reforming catalyst generated 0.42 W cm^{-2} at 850°C using 10% EtOH/Ar (balance) [41]. Compared to these state-of-art SOFCs, MS-SOFCs with HEA-SDC reforming catalysts showed significant improvement.
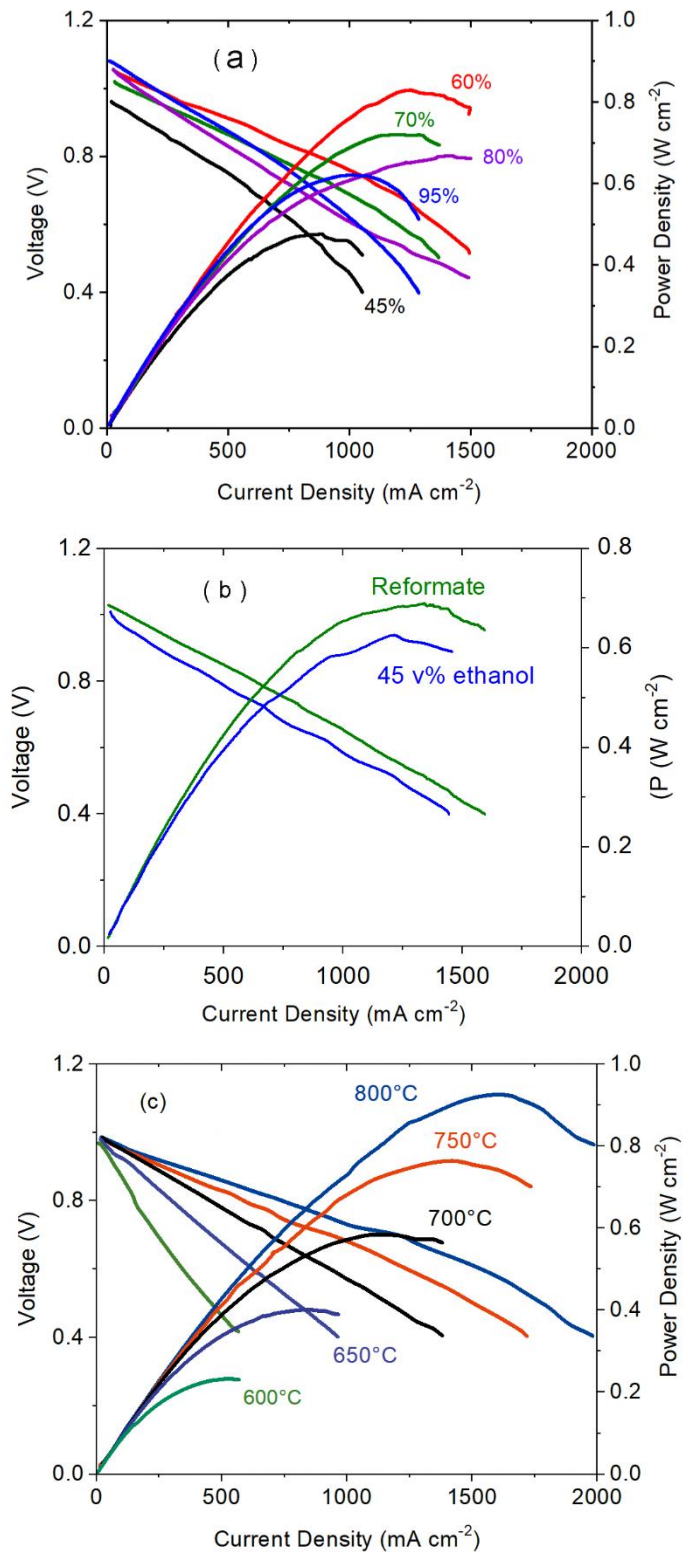
Fig. 4. Evaluation of HEA loading, internal reforming efficiency and cell performance at different ethanol concentrations and operating temperature. a: VI-PI curves at 45 to 95% EtOH

concentrations at 700°C, b: VI-PI curves of a MS-SOFC tested with 45% EtOH and simulated reformate gas representing the same 45% EtOH fuel reformate at 700°C, c: VI-PI curves of a MS-SOFC tested at a temperature range of 600 to 800°C. Other cell testing conditions: fuel flow: 6 mL h^{-1} 60% EtOH, air flow:1.2 L/min.

3.3. **Mass Transport in Optimized Cells**

Oxygen and hydrogen mass transport have been evaluated using the method of Fukuyama et al., in which polarization curves are obtained over a range of reactant concentrations, and the limiting current is evaluated to quantify the mass transport [42]. The IV curves using 10% H_2/N_2 (balance) and 97% H_2/N_2 are straight lines, indicating that hydrogen supply was sufficient to keep a high current density of 1.7 A cm^{-2} and 2.2 A cm^{-2}, respectively (Fig. 5a). The hydrogen mass transport resistance ($R_{H2, HEA}$) was determined to be 26.2 sec m^{-1} based on the limiting current for 5% H_2, a low resistance even with the addition of the HEA layer, visible in Fig. 5c. This $R_{H2, HEA}$ is slightly higher than the $R_{H2, Ni-SDC}$ (21.5 s m^{-1}) for a similar anode without HEA added, and much lower than the oxygen-side mass transport resistance R_{O2} (44.2 s m^{-1}); addition of HEA does not significantly impact the mass transport limitation for these cells [32]. Note that the hydrogen concentration expected for fully reformed 60% EtOH is 58.1%, well within the range for minimal mass transport restriction. The thin and porous HEA-SDC layer (~20 μm) provided sufficient hydrogen transport to obtain the high power (0.83 W cm^{-2}) via steam reforming (Fig. 4a). The improved mass transport was supported by the porous HEA structure formed during fast firing and additional porosity formed during reduction in hydrogen. The highly porous Pr_6O_{11} nanoelectrode (Fig. 5d) provides smooth and efficiency oxygen transfer. The IV curves using 21 to 100% O_2/N_2 did not show significant mass transport restriction (Fig. 5b). Limiting current behavior was

observed for 10% O_2/N_2 and lower oxygen concentration. The oxygen mass transport resistance (RO_2) was determined to be 42.6 sec m^{-1} based on the limit current for 5% O_2/N_2. Oxygen mass transport is more limiting than hydrogen mass transport, consistent with our previous work that focused on improving air-side mass transport by optimizing the metal support structure [32]. Using pure oxygen at the cathode, the Pmax reached 1.5 W cm^2 using 70 % EtOH (Fig. S8), indicating the high reforming efficiency of the HEA-SDC catalyst supports a higher current density than observed with air, and possible future improvement in cell performance if the oxygen electrode can be further improved for mass transport.
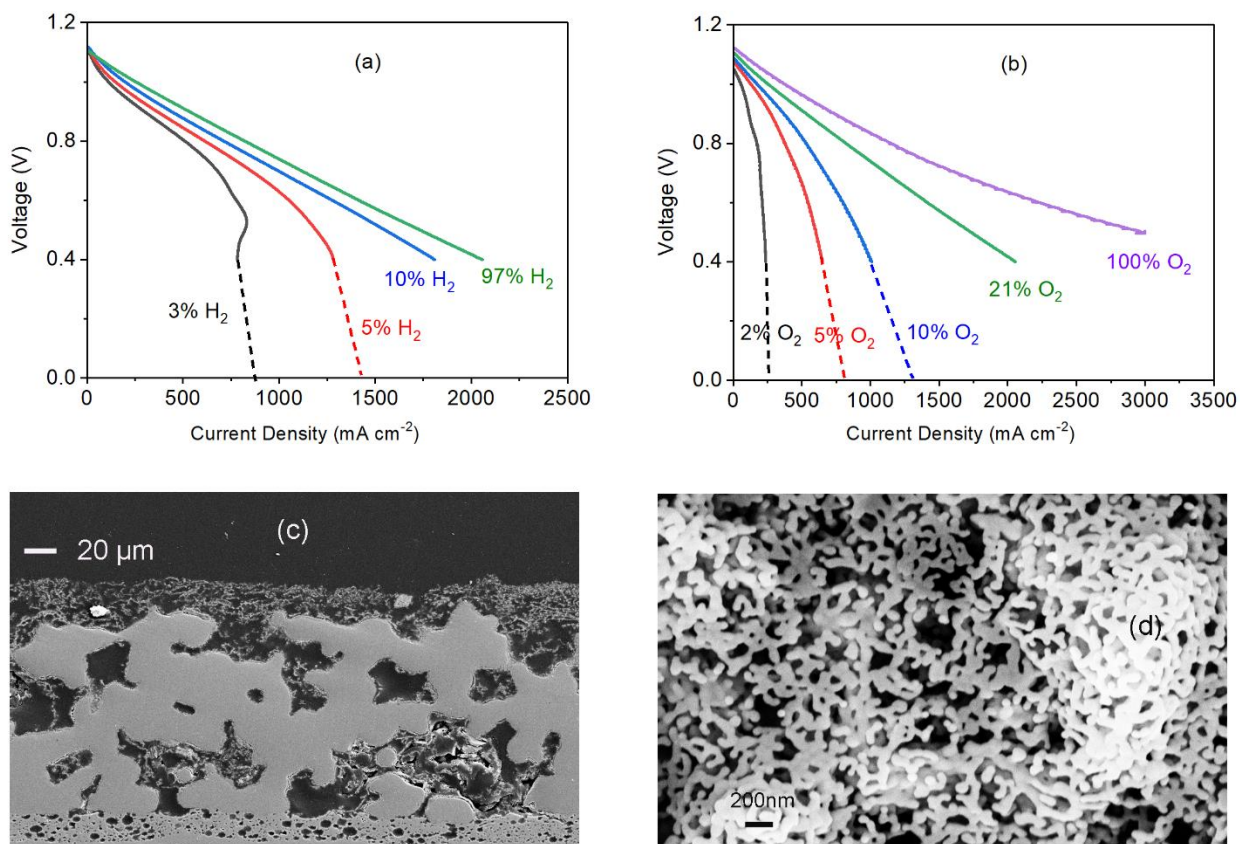
Fig. 5. Mass transport measurement and cell structure. V-I curves at 700°C with various concentrations of (a) H_2, and (b) O_2. (c) Cross-section SEM image of the anode electrode and metal

support with 20-30 µm HEA-SDC reforming catalyst visible on top of the metal support. (d) Porous Pr_6O_{11} cathode catalyst in the ScSZ electrode scaffold.

3.4. Cell Stability & Alternate Fuels

An optimized MS-SOFC demonstrated stable short-term operation at 0.7 W cm^{-2} using 60% EtOH fuel at 700°C and 0.7 V and current density around 1 A cm^{-2} (Fig. 6a). The current density fluctuations arise from small variations in fuel supply rate due to pumping and evaporation transients. Cells operated for approximately 90 h or longer with 45% EtOH, 45% EtOH simulated reformate gas, 60% EtOH, and hydrogen baseline showed similar degradation rates (Fig. 6b). For 60% EtOH, the average degradation rate over 87 h was 18.5%/100 h, which is similar to reformate (18.2%/100 h) and 45% EtOH (18.7%/100 h). Degradation with hydrogen baseline was a bit slower, at 13%/100h. This suggests that degradation of the HEA catalyst may be slightly faster than other cell degradation modes (such as electrocatalyst coarsening and Cr deposition in the cathode). Addition of carbon-containing species to the gas composition and DIR do not appear to dramatically impact degradation. This is consistent with previous results for gaseous fuels including reformed natural gas, ammonia and dimethyl ether [2, 43].

For the consumer vehicle application, rapid start-up capability is critical. Thermal cycling tolerance of the cell and electrocatalysts is well established [8, 44, 45]. Here, thermal cycling tolerance of the HEA was additionally demonstrated by subjecting a cell to 5 thermal cycles (700-250-700°C, heating ramp rate 25°C/min) separated by 100 h continuous operation in 45% EtOH fuel. Severe carbon deposition is expected for ethanol fuel in the range 400 to 630°C, so the fuel was switched to hydrogen during heating and cooling. Performance with both hydrogen and

ethanol was determined after each set of thermal cycle plus 100 h continuous operation. Stable OCVs were demonstrated in hydrogen fuel and ethanol fuel, indicating the cell had no leak during 500 h and 5 thermal cycles (Fig. 6c). Most degradation occurs during the first 100 h test, which was attributed to catalyst coarsening (Section 3.5). The cell performance was relatively stable for 300 h after the second thermal cycle (Figs. 6d, S9).
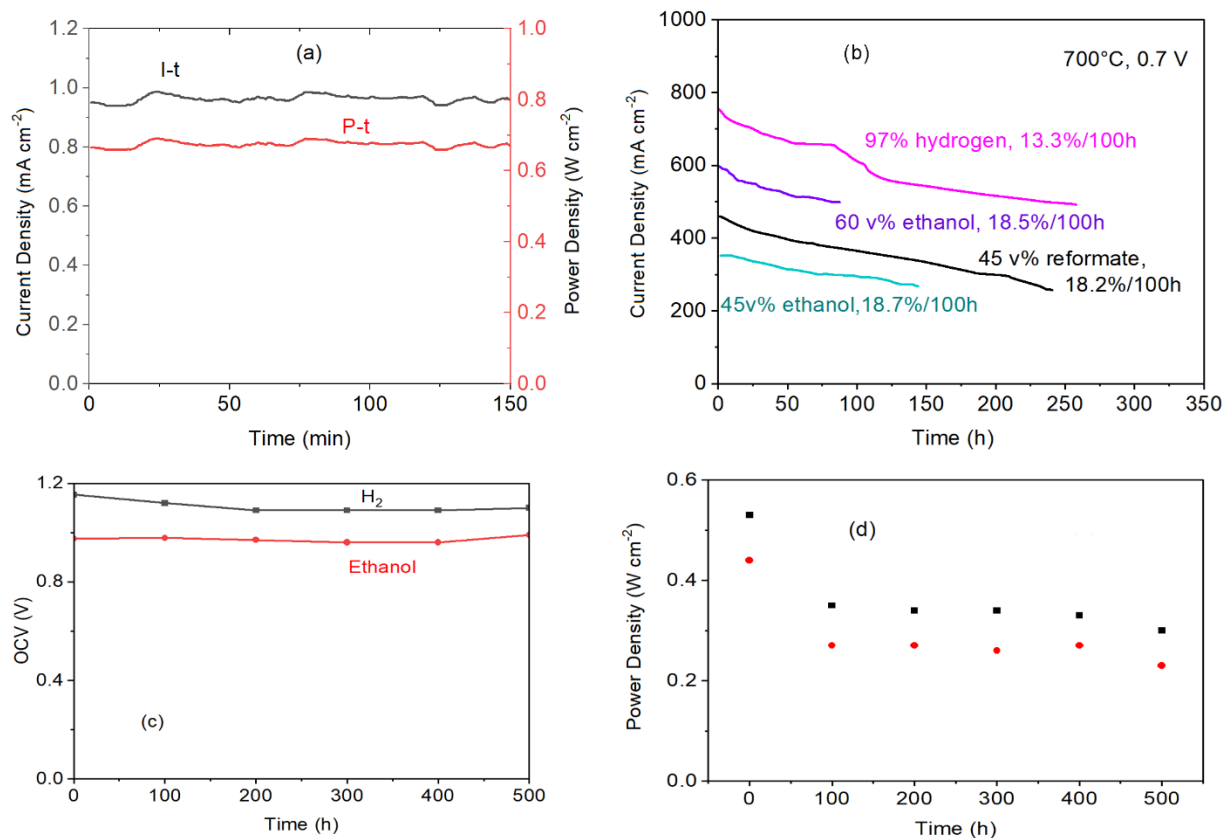

Fig. 6. Stability of internal reforming HEA-SDC-Ni anode-based MS-SOFCs with ethanol fuels. (a) Short-term stability of one best-performing cell. (b) Comparison of MS-SOFC cell stability with 45% EtOH, 45% EtOH simulated reformate gas, 60% EtOH, and hydrogen fuels. (c) OCV and (d) power at 0.7 V in hydrogen fuel and 45% EtOH fuel after thermal cycles (250°C-700°C-250°C, cooling in N_2).

Cells were also operated with methanol and denatured ethanol to demonstrate a range of fuel compositions and impurities. A cell operated with 60 v% methanol obtained a P_{max} of 0.71 W cm^{-1} (Fig. S10a). The cell demonstrated no degradation during 50 h operation with 60 v% SDA-3A (which contains methanol and ethanol in a volume ratio of 5:100, Fig S11). Direct methanol fueled SOFC cells were reported without degradation for about 40 hours in Hu et al[3] and Ru et al[46]. respectively. Methanol fueled SOFCs had better stability than ethanol fueled SOFCs [46]. Therefore, addition of a small amount of methanol to ethanol is not expected compromise performance or stability. Our operation with denatured ethanol is described in detail elsewhere [47], and the critical results are reproduced in Fig. S11. Briefly, good performance and stability was achieved with denatured ethanol, using methanol, isopropanol, and denatonium benzoate denaturants. In contrast, using gasoline as the denaturant caused fast degradation due to carbon deposits in the anode.

3.5 Posttest Analysis

The absence of carbon deposits in posttest HEA-containing anodes operated at 700°C with 60% EtOH or 45% EtOH reformates for >100 h was confirmed by Raman analysis (Fig. 7a). In contrast, obvious carbon deposits (D, 2D, and G peaks in Fig. 7a) were observed on Ni-SDC anode-based MS-SOFCs without HEA after 24 h operation in 60% EtOH fuel (Fig. 3b and 7c). Ni is known to promote carbon deposition [48]. A peak at 553 and 1100 cm^{-1} is assigned NiO. A peak at 465 cm^{-1} is assigned to CeO_2. A peak at 623 cm^{-1} is assigned to Co_2O_3. More Raman spectra of posttest HEA-SDC-Ni anode-based MS-SOFC tested in a simulated reformate of 45% EtOH also show that HEA is resistive to carbon formation (Fig. S12).

SEM-EDS detected 1.2 atm% of Cr at Pr_6O_{11} cathode near ScSZ electrolyte after ~100 h cell test in 60% EtOH-air (Fig. 7b). Compared to a pretest cathode (fresh cell) with 1 atom% Cr, a small increase (0.2 atom%) was observed in post-test metal supported cells.

Posttest characterization shows Ni agglomeration in the Ni-SDC anode and HEA layer (Fig. 7c and Fig. S13)). Comparing the fresh (Fig. S13e) and posttest (Fig. S13a) Ni-SDC anode, Ni segregation was observed. Presumably, Ni segregation led to loss of active catalyst surface area and contributed to cell degradation. This is consistent with previous observations of Ni coarsening in MS-SOCs [2, 49]; Ni coarsening is a fundamental feature of the infiltrated anode and does not appear to be significantly impacted by internal reforming of ethanol. Overall, combined effects of chromia deposition, carbon formation, and Ni aggregation contributed to the cell degradation [50]. Protective layers on metal support are being developed to mitigate chromia evaporation and further improve the cell stability.
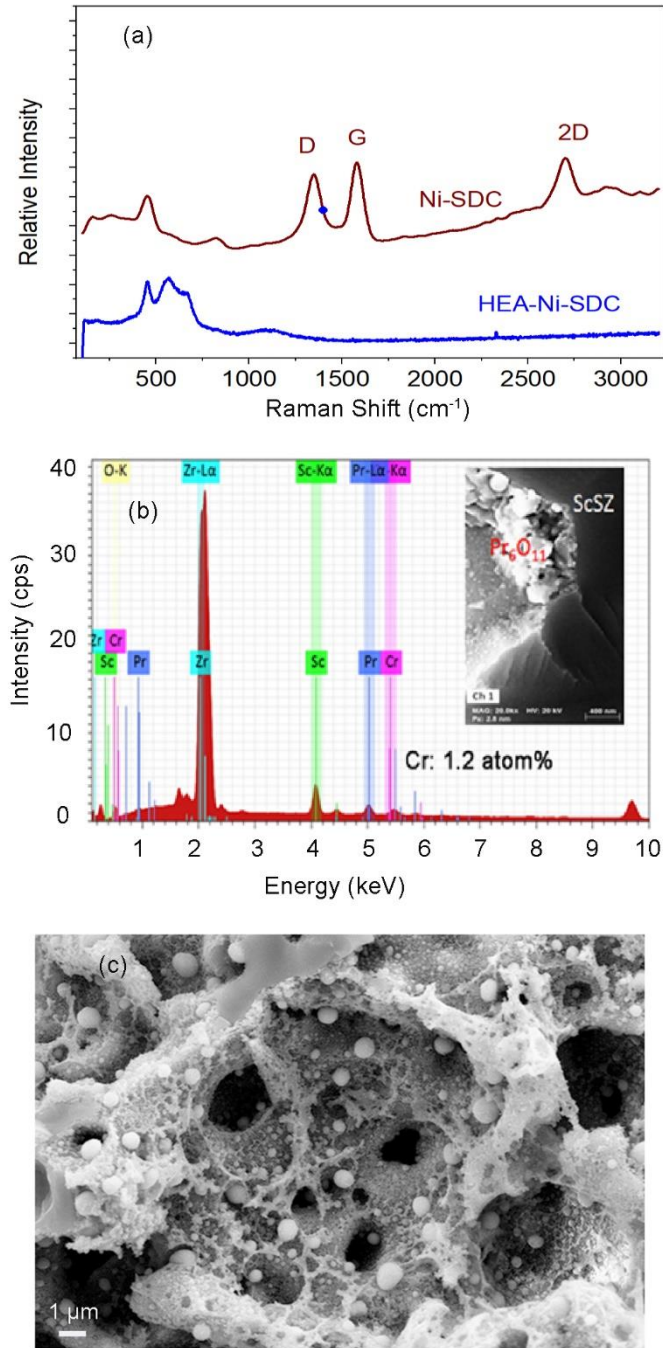
Fig. 7. Posttest analysis of 60% ethanol-fueled MS-SOFCs after ~100 h of operation at 700°C. a: Raman spectra of anodes with and without HEA. b: SEM-EDS of the Pr_6O_{11} cathode near ScSZ electrolyte, c: SEM image of posttest HEA-SDC-Ni anode near metal support.

3.6. Thermodynamic Calculations for Predicting Carbon Formation

The impact of ethanol/steam ratio on reformed gas composition and carbon deposition was obtained from thermodynamic analysis using open-source Cantera (version 2.4) and Python (version 3.7) software. Carbon formation gradually decreases with an increase of steam/ethanol molar ratio from 1.2 to 2 at the equilibrium state of the steam/ethanol reforming reaction (Fig. 8a). At 700°C or above, carbon will not be present for ethanol/steam ratio >1.6 (≤70% EtOH). To avoid carbon formation at lower temperature zones (including inlet and outlet tubes), a high steam/ethanol molar ratio (>2) is recommended. Carbon is not formed at 650°C or higher for 60% EtOH (steam/ethanol: 2.16:1), which is consistent with the Raman analysis results of posttest HEA anode (Fig.8a). Theoretically, 45% EtOH (steam/ethanol: 3.81:1) will not form any carbon deposit at >250°C (Fig S14, a). this was also confirmed by Raman analysis (Fig. S12). However, small amount of amorphous carbon arisen from catalytic metal support (Fig. S12) although Ni-SDC coatings mitigated the exposure. The HEA catalyst has proved to be a key factor for mitigating carbon deposition. Carbon is not predicted to form above 700°C at 45 to 70% EtOH (steam/ethanol ≥ 1.7 in molar) as discussed below in Fig. 8a. Furthermore, the incomplete reforming in the absence of HEA means the actual gas composition in the Ni-SDC anode deviates from the equilibrium reformed composition considered in the thermodynamic calculation. HEA catalyst has much less nickel content, promotes reforming to the thermodynamically expected gas composition, and the mixed-valent copper/manganese enhances CO oxidation and water-gas shift reaction, mitigating carbon formation.

For steam reforming of 60% EtOH the predicted hydrogen concentration reaches a maximum at about 700°C (Fig. 7b), suggestion that the optimal operating temperature is between 700-750°C. This temperature range is also good for avoiding rapid metal support oxidation [51, 52]. Hydrogen

concentration in the anode varies with the ethanol fuel concentration. The hydrogen mole fraction at 45% EtOH is 0.53, compared to 0.58 at 60% EtOH (Table S1), leading to a theoretical OCV of 1.0 V and 1.04 V, respectively. Increase in hydrogen fraction at high ethanol concentration contributes to a higher cell performance (Fig. 4a). The calculated gas compositions of 45% EtOH reformate to those for 60 v% methanol, and they have the same hydrogen fractions at 700°C (Fig. S14). These calculated results explain why the performance with 45% EtOH and 60 v% methanol is very similar (0.71 W cm^{-2}) in Figs. S5 and S10.
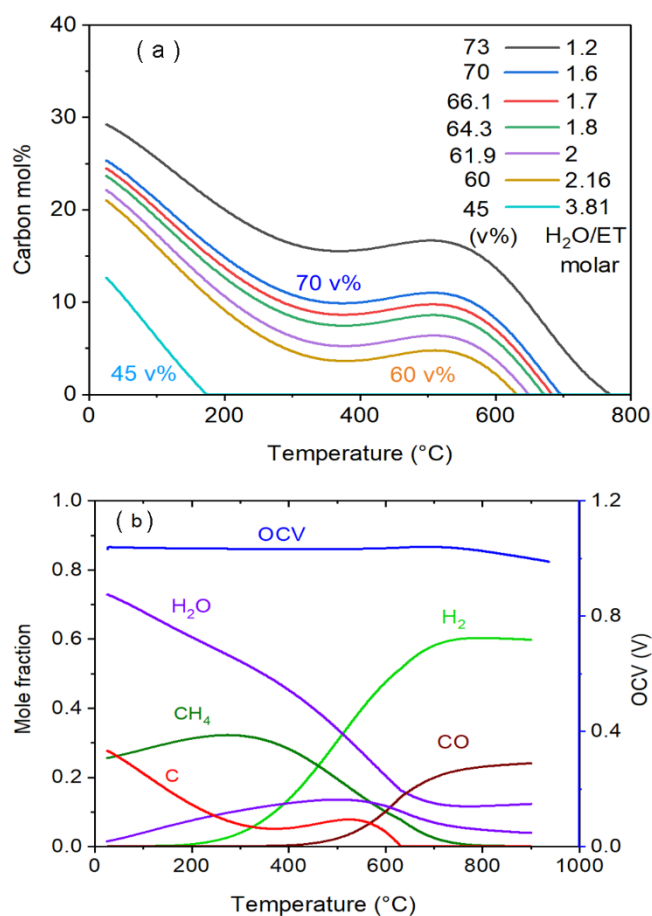
Fig. 8. Carbon deposition and gas composition equilibria of steam reforming of ethanol at various fuel/steam ratios and temperatures. (a) Ethanol concentration effect on carbon mole fraction. (b) composition equilibria of steam reforming of 60% EtOH fuel.

5. Conclusions

Ethanol-fueled MS-SOFCs with HEA-SDC internal reforming catalyst have been developed for electricity generation. For 60% EtOH, addition of HEA-SDC DIR catalyst improved cell performance by 34%, prevented carbon deposition, and extended the lifetime compared to standard Ni-SDC anode. For coating HEA in the metal support/anode side, the infiltration method was found to be better than the painting method. Optimal HEA/SDC weight ratio (60:40) and catalyst loading weight (6 mg cm^{-2}) were confirmed by cell testing. For the optimal operating conditions at 700°C, 60% EtOH fuel delivered a maximum power of 0.83 W cm^{-2} at optimal fuel flow rate of 6 mL min^{-1} and air flow of 1.2 L min^{-1}. Mass transport in both electrodes was quantified (R_{O2}: 42.6 sec m^{-1} and R_{H2}: 26.2 sec m^{-1}), an oxygen mass transport limits cell performance. Ethanol-fueled MS-SOFCs demonstrated 5 thermal cycles without leaking, and OCV was stable. After 100 h initial break-in, stable operation was achieved for 300 h. Similar performance and durability is shown for methanol, and ethanol fuels denatured with methanol or isopropanol. Thermal dynamic analysis predicts carbon deposition does not occur during normal operating conditions, which is supported by post-test analysis by Raman spectroscopy.

Acknowledgements

References

[1] A. Weber, Fuel Cells, 21 (2021) 440-452.

[2] M.M. Welander, B. Hu, M.C. Tucker, Inter. J. Hydrogen Energy, 47 (2022) 11261-11269.

[3] B. Hu, M. Keane, K. Patil, M.K. Mahapatra, U. Pasaogullari, P. Singh, Appl. Energy, 134 (2014) 342-348.

[4] J.O. Christensen, B.R. Sudireddy, A. Hagen, ECS Trans., 103 (2021) 713-724.

[5] Q. Fang, L. Blum, P. Batfalsky, N.H. Menzler, U. Packbier, D. Stolten, Int. J. Hydrogen Energy, 38 (2013) 16344-16353.

[6] M. Dewa, M.A. Elharati, A.M. Hussain, Y. Miura, D. Song, Y. Fukuyama, Y. Furuya, N. Dale, X. Zhang, O.G. Marin-Flores, D. Wu, M.G. Norton, S. Ha, J. Power Sources, 541 (2022).

[7] E. Dogdibegovic, Y. Fukuyama, M.C. Tucker, J. Power Sources, 492 (2021).

[8] M.C. Tucker, J. Power Sources, 395 (2018) 314-317.

[9] M.C. Tucker, B. Carreon, J. Charyasatit, K. Langston, C. Taylor, J. Manjarrez, N. Burton, M. LaBarbera, C.P. Jacobson, ECS Trans., 57 (2013) 503-509.

[10] M.C. Tucker, A.S. Ying, Int. J. Hydrogen Energy, 42 (2017) 24426-24434.

[11] S. Ma, X. Hu, Y. Zhao, X. Wang, C. Dong, ACS Omega, 6 (2021) 29201-29214.

[12] M.A. Elharati, M. Dewa, Q. Bkour, A. Mohammed Hussain, Y. Miura, S. Dong, Y. Fukuyama, N. Dale, O.G. Marin-Flores, S. Ha, Energy Technol., 8 (2020).

[13] F. de Oliveira Gonçalves, E. Savioli Lopes, M. Savioli Lopes, R. Maciel Filho, Int J Hydrogen Energy, 46 (2021) 36381-36397.

[14] G. Avgouropoulos, T. Ioannides, J.K. Kallitsis, S. Neophytides, J. Chem. Eng., 176-177 (2011) 95-101.

[15] Stephen H. Clarke, Andrew L. Dicks, Kevin Pointon, Thomas A. Smith, A. Swann, Catal. Today, 38 (1997) 411-423.

[16] S. Assabumrungrat, V. Pavarajarn, S. Charojrochkul, N. Laosiripojana, Chem. Eng. Sci, 59 (2004) 6015-6020.

[17] C. Schluckner, V. Subotić, V. Lawlor, C. Hochenauer, J. Electrochem. Soc., 163 (2016) F761-F770.

[18] P. Boldrin, E. Ruiz-Trejo, J. Mermelstein, J.M. Bermudez Menendez, T. Rami Rez Reina, N.P. Brandon, Chem Rev, 116 (2016) 13633-13684.

[19] A. Cherif, N. Doner, F. Şen, Catalysts for high-temperature fuel cells operated by alcohol fuels, in: Nanomaterials for Direct Alcohol Fuel Cells, 2021, pp. 173-186.

[20] S. Ogo, Y. Sekine, Fuel Process. Technol, 199 (2020).

[21] L. Yang, Y. Choi, W. Qin, H. Chen, K. Blinn, M. Liu, P. Liu, J. Bai, T.A. Tyson, M. Liu, Nat Commun, 2 (2011) 357.

[22] W. Wang, Y. Chen, F. Wang, M.O. Tade, Z. Shao, Chem. Eng. Sci., 126 (2015) 22-31.

[23] S. Park, J.M. Vohs, R.J. Gorte, Nature, 404 (2000) 265-267.

[24] Shung-Ik Lee, Kipyung Ahn, John M. Vohs, R.J. Gorte, Electrochem. solid-state lett., 8 (2005) 48-51.

[25] R. Gorte, Solid State Ion., 175 (2004) 1-6.

[26] B.J.M. Sarruf, J.-E. Hong, R. Steinberger-Wilckens, P.E.V. de Miranda, Int. J. Hydrogen Energy, 43 (2018) 6340-6351.

[27] P. Zhang, L. Hu, B. Zhao, Z. Lei, B. Ge, Z. Yang, X. Jin, S. Peng, Fuel, 333 (2023).

[28] A. Salcedo, P.G. Lustemberg, N. Rui, R.M. Palomino, Z. Liu, S. Nemsak, S.D. Senanayake, J.A. Rodriguez, M.V. Ganduglia-Pirovano, B. Irigoyen, ACS Catal., 11 (2021) 8327-8337.

[29] D.B. Miracle, Nat. Commun., 10 (2019) 1805.

[30] K.X. Lee, B. Hu, P.K. Dubey, M.R. Anisur, S. Belko, A.N. Aphale, P. Singh, Int. J. Hydrogen Energy, 47 (2022) 38372-38385.

[31] M. Dewa, W. Yu, N. Dale, A.M. Hussain, M.G. Norton, S. Ha, Int J Hydrogen Energy, 46 (2021) 33523-33540.

[32] B. Hu, G. Lau, D. Song, Y. Fukuyama, M.C. Tucker, J. Power Sources, 555 (2023).

[33] L. Zhang, W. Cai, N. Bao, Adv Mater, 33 (2021) e2100745.

[34] D. Berardan, A.K. Meena, S. Franger, C. Herrero, N. Dragoe, J. Alloys Compd., 704 (2017) 693-700.

[35] T. Li, Y. Yang, X. Wang, K. Zheng, S. Shen, X. Ou, B. Lin, P. Feng, S. Wang, Y. Ling, J. Power Sources, 512 (2021).

[36] T. Tan, M. Qin, K. Li, M. Zhou, T. Liu, C. Yang, M. Liu, Int. J. Hydrogen Energy, 45 (2020) 29407-29416.

[37] P. Sivakumar, R. Ramesh, A. Ramanand, S. Ponnusamy, C. Muthamizhchelvan, Mater. Lett., 65 (2011) 1438-1440.

[38] A. Hagen, X. Sun, B.R. Sudireddy, Å.H. Persson, ECS Trans., 91 (2019) 867-876.

[39] E.N. Armstrong, J.-W. Park, N.Q. Minh, Electrochem. solid-state lett., 15 (2012).

[40] A. Arpornwichanop, N. Chalermpanchai, Y. Patcharavorachot, S. Assabumrungrat, M. Tade, Int J Hydrogen Energy, 34 (2009) 7780-7788.

[41] M.C. Steil, S.D. Nobrega, S. Georges, P. Gelin, S. Uhlenbruck, F.C. Fonseca, Appl. Energy, 199 (2017) 180-186.

[42] Y. Fukuyama, T. Shiomi, T. Kotaka, Y. Tabuchi, Electrochim. Acta, 117 (2014) 367-378.

[43] M.M. Welander, B. Hu, S. Belko, K.X. Lee, P.K. Dubey, I. Robinson, P. Singh, M.C. Tucker, Int. J. Hydrogen Energy, 48 (2023) 1533-1539.

[44] E. Dogdibegovic, Y. Cheng, F. Shen, R. Wang, B. Hu, M.C. Tucker, J. Power Sources, 489 (2021).

[45] M.C. Tucker, Int. J. Hydrogen Energy, 43 (2018) 8991-8998.

[46] Y. Ru, J. Sang, C. Xia, W.-C.J. Wei, W. Guan, Int. J. Hydrogen Energy, 45 (2020) 7069-7076.

[47] B. Hu, M.C. Tucker, ECS Trans. , 111 (2023) 1481-1486.

[48] J. Xiao, Y. Xie, J. Liu, M. Liu, J. Power Sources, 268 (2014) 508-516.

[49] F. Shen, R. Wang, M.C. Tucker, J. Power Sources, 474 (2020).

[50] K.N. Grew, A.S. Joshi, W.K.S. Chiu, Fuel Cells, 10 (2010) 1143-1156.

[51] F. Shen, M.M. Welander, M.C. Tucker, Int. J. Hydrogen Energy, 48 (2023) 12168-12175.

[52] M. Reisert, V. Berova, A. Aphale, P. Singh, M.C. Tucker, Int. J. Hydrogen Energy, 45 (2020) 30882-30897.